

Dislocation Formation and Work-Hardening in Two-Phase Alloys

Akihiko Minami and Akira Onuki
Department of Physics, Kyoto University, Kyoto 606-8502, Japan
(Dated: December 2, 2024)

A phase field model is presented to investigate dislocation formation (coherency loss) and work-hardening in two-phase binary alloys. In our model the elastic energy density is a periodic function of the shear and tetragonal strains, which allows multiple formation of slips (dislocation dipoles). By numerically integrating the dynamic equations in two dimensions, we find that dislocations appear in pairs in the interface region and grow into slips. One end of each slip glides preferentially into the softer region, while the other end remains trapped at the interface. Under uniaxial stretching at deep quenching, slips appear in the softer regions and do not penetrate into the harder domains, giving rise to an increase of the stress with increasing applied strain in plastic flow.

I. INTRODUCTION

In crystalline solids many kinds of phase transformations are strongly influenced by the elastic field^{1,2,3,4}. Since the first work by Cahn^{5,6} most theoretical studies have been focused on the coherent case in which the lattice planes are continuous through the interfaces. In the incoherent case, on the other hand, dislocations appear around the interfaces giving rise to coherency loss¹. Incoherent microstructures have been observed in various alloys when the lattice constants or the crystalline structures of the two phases are not very close^{7,8}. Theory in the incoherent case has been much more difficult, obviously because the effects cannot be described within the usual linear elasticity theory⁹. The aim of this paper is hence to present a simple mathematical model reasonably describing the incoherent effects in binary alloys. Use will be made of a recent nonlinear elasticity theory of plastic flow by one of the present authors¹⁰.

A number of authors have studied composition changes around dislocations fixed in space and time, which lead to a compositional Cottrell atmosphere¹¹ or preferential nucleation around a dislocation^{12,13}. As recent numerical work in two dimensions, phase separation has been studied by Léonard and Desai¹⁴ and by Hu and Chen¹⁵ using a continuum Ginzburg-Landau or phase field model in the presence of fixed dislocations. In these papers, dislocations preexist as singular objects before composition changes. We also mention atomistic simulations of dislocation motion influenced by diffusing solutes¹⁶ or by precipitated domains¹⁷.

Mechanical properties of two-phase solids can be very different from those of one-phase solids^{7,11,18}. These effects are important in technology, but have rarely been studied theoretically. For example, in plastic flow with high-density dislocations in two-phase states, the stress or the apparent shear modulus increases with increasing the strain, which is called the work-hardening effect. One main origin is that dislocation loops are pinned at precipitated domains. This will indeed be the case in our simulation.

This paper is organized as follows. In Section 2 we will present the free energy functional for the composition

and the elastic field, in which the elastic energy density is a periodic function of the tetragonal and shear strains. In Section 3 we will construct dynamical equations. In Section 4 numerical results will be given on the dislocation formation around domains and on the stress-strain relations under uniaxial stretching.

II. FREE ENERGY FUNCTIONAL

We consider a binary alloy consisting two components, *A* and *B*, neglecting vacancies and interstitials. The compositions, c_A and c_B , of the two components satisfy $c_A + c_B = 1$. In real metallic alloys undergoing a phase transition, there can be a change in the atomic configuration within unit cells as well as in the overall composition, resulting in precipitates with the so-called $L1_0$ or $L1_2$ structure, for example^{2,4,19}. In this paper the composition difference is the order parameter,

$$\psi = c_A - c_B. \quad (2.1)$$

The other variables representing the order-disorder phase transition are neglected. Then ψ is defined in the range $-1 \leq \psi \leq 1$ and

$$c_A = \frac{1}{2}(1 + \psi), \quad c_B = \frac{1}{2}(1 - \psi). \quad (2.2)$$

In our free energy $F = \int dr f$ the order parameter ψ and the elastic displacement \mathbf{u} are coupled. The free energy density f is of the form,

$$f = f_{\text{BW}}(\psi) + \frac{C}{2}|\nabla\psi|^2 + \alpha e_1 \psi + f_{\text{el}}. \quad (2.3)$$

The first term is the Bragg-Williams free energy density expressed as⁴,

$$\begin{aligned} \frac{v_0}{k_B T} f_{\text{BW}} &= \frac{1 + \psi}{2} \ln(1 + \psi) + \frac{1 - \psi}{2} \ln(1 - \psi) \\ &\quad - T_0 \psi^2 / 2T, \end{aligned} \quad (2.4)$$

where v_0 is the volume of a unit cell representing the atomic volume, T_0 is the mean-field critical temperature

in the absence of the coupling to the elastic field. If $|\psi| \ll 1$, we obtain the Landau expansion $v_0 f_{\text{BW}}/k_B T = (1 - T_0/T)\psi^2/2 + \psi^4/24 + \dots$. However, we will not use this form because we are interested in the deeply quenched case. The second term in (2.3) is the gradient term where C is a constant of order $k_B T_0/v_0^{1/3}$. The parameter α represents the strength of the coupling between the composition and the dilation strain $e_1 = \nabla \cdot \mathbf{u}$. This coupling arises in the presence of a difference in the atomic sizes of the two species and is consistent with the empirical fact that the lattice constant changes linearly as a function of the average composition in many one-phase alloys (Vegard law). It gives rise to a difference in the lattice constants of the two phases in phase separation (lattice misfit). It also explains a composition inhomogeneity (Cottrell atmosphere or nucleating precipitate) around a dislocation.

In two dimensions f_{el} depends on the following strains,

$$\begin{aligned} e_1 &= \nabla_x u_x + \nabla_y u_y, \\ e_2 &= \nabla_x u_x - \nabla_y u_y, \\ e_3 &= \nabla_y u_x + \nabla_x u_y. \end{aligned} \quad (2.5)$$

The elastic displacement \mathbf{u} is measured in a reference one-phase state at the critical composition. We call e_2 the tetragonal strain and e_3 the shear strain. In this paper we use a nonlinear elastic energy density of the form,

$$f_{\text{el}} = \frac{1}{2} K e_1^2 + \Phi(\psi, e_2, e_3). \quad (2.6)$$

The first term represents the elastic energy due to dilation with K being the bulk modulus. The second term arises from anisotropic shear deformations defined for arbitrary values of e_2 and e_3 . Assuming a square lattice structure¹⁰, we set

$$\Phi = \frac{\mu_2}{4\pi^2} [1 - \cos(2\pi e_2)] + \frac{\mu_3}{4\pi^2} [1 - \cos(2\pi e_3)]. \quad (2.7)$$

The principal crystal axes are along or make angles of $\pm\pi/4$ with respect to the x or y axis. In Fig.1 we plot Φ as a function of e_2 and e_3 for the case $\mu_2 = \mu_3 = \mu_0$ in units of μ_0 . If the system is homogeneous, elastic stability is attained for $\partial^2 \Phi / \partial e_2^2 > 0$ and $\partial^2 \Phi / \partial e_3^2 > 0$ or in the regions $|e_2 - n| < 1/4$ and $|e_3 - m| < 1/4$ with n and m being integer values¹⁰.

For small strains $|e_2| \ll 1$ and $|e_3| \ll 1$, it follows the usual standard form⁹,

$$\Phi \cong \frac{1}{2} \mu_2 e_2^2 + \frac{1}{2} \mu_3 e_3^2, \quad (2.8)$$

in the linear elasticity theory. Therefore,

$$\mu_2 = \frac{1}{2} (C_{11} - C_{12}), \quad \mu_3 = C_{44}, \quad (2.9)$$

in terms of the usual elastic moduli C_{11} , C_{12} , and C_{44} ⁹. In the original theory⁵ the isotropic linear elasticity with

constant $\mu_2 = \mu_3$ was assumed. Subsequent theories treated the case of the cubic linear elasticity with constant μ_2 and μ_3 ^{2,3,4,6,20}. In the present paper, while K is a constant, μ_2 and μ_3 depend on the composition as^{4,21,22}

$$\mu_2 = \mu_{20} + \mu_{21}\psi, \quad \mu_3 = \mu_{30} + \mu_{31}\psi. \quad (2.10)$$

If $\mu_{21} > 0$ and $\mu_{31} > 0$, the regions with larger (smaller) ψ are harder (softer) than those with smaller (larger) ψ . This *elastic inhomogeneity* gives rise to asymmetric elastic deformations in two-phase structures and eventual pinning of the domain growth.

In our theory $\Phi(\psi, e_2, e_3)$ in (2.7) is the simplest periodic function of e_2 and e_3 with period 1. The periodicity arises from the fact that the square lattice is invariant with respect to a slip of the crystal structure by a unit lattice constant along a line parallel to the x or y axis. Notice that, under rotation of the reference frame by θ , e_2 and e_3 are changed to e'_2 and e'_3 , respectively, with¹⁰

$$\begin{aligned} e'_2 &= e_2 \cos 2\theta + e_3 \sin 2\theta, \\ e'_3 &= -e_2 \sin 2\theta + e_3 \cos 2\theta. \end{aligned} \quad (2.11)$$

For $\theta = \pi/2$ we have $e'_2 = -e_2$ and $e'_3 = -e_3$, so f_{el} in (2.7) remains invariant. For $\theta = \pi/4$ we have $e'_2 = e_3$ and $e'_3 = -e_2$ and recognize that the roles of tetragonal and shear strains are exchanged. For $\mu_2 = \mu_3$, the linear elasticity in (2.8) becomes isotropic, but the nonlinear elasticity is still anisotropic (from the fourth-order terms in the expansion of Φ in (2.7) in powers of e_2 and e_3).

The elastic stress tensor $\vec{\sigma} = \{\sigma_{ij}\}$ is expressed as

$$\begin{aligned} \sigma_{xx} &= K e_1 + \alpha \psi + \mu_2 \sin(2\pi e_2)/2\pi, \\ \sigma_{yy} &= K e_1 + \alpha \psi - \mu_2 \sin(2\pi e_2)/2\pi, \\ \sigma_{xy} &= \sigma_{yx} = \mu_3 \sin(2\pi e_3)/2\pi, \end{aligned} \quad (2.12)$$

where one of the crystal axes is parallel to or makes an angle of $\pi/4$ with respect to the x axis. In the linear elasticity $\sin(2\pi e_2)/2\pi$ and $\sin(2\pi e_3)/2\pi$ are replaced by e_2 and e_3 , respectively. Notice the relation,

$$\nabla \cdot \vec{\sigma} = -\frac{\delta}{\delta \mathbf{u}} F, \quad (2.13)$$

where ψ is fixed in the functional derivative $\delta F / \delta \mathbf{u}$.

The mechanical equilibrium condition $\nabla \cdot \vec{\sigma} = \mathbf{0}$ is equivalent to the extremum condition $\delta F / \delta \mathbf{u} = \mathbf{0}$. For shallow quenching this condition may be assumed even in dynamics. In fact, using this condition in the linear elasticity, the elastic field has been expressed in terms of ψ in the previous theories (see the appendix)^{1,2,3,4,5,6}. (i) The typical strain around domains is given by⁴

$$e_0 = \alpha \Delta c / L_0, \quad (2.14)$$

where $\Delta c = \Delta \psi / 2$ is the composition difference between the two phases and

$$L_0 = K + \mu_{20} \quad (2.15)$$

is the longitudinal elastic modulus. This strain needs to be small ($e_0 < 1/4$ approximately) in the coherent condition. (ii) As will be shown in the the appendix, in the limit of weak cubic elasticity and weak elastic inhomogeneity, one-phase states become linearly unstable for $k_B(T - T_0)/2v_0 < \alpha^2/2L_0$ or for $T < T_s$ with

$$T_s = T_0 + v_0 \alpha^2 / L_0 k_B. \quad (2.16)$$

(iii) Furthermore, (A.5) suggests that the typical domain size in steady pinned states is a decreasing function of the quench depth $T_s - T$.

III. DYNAMIC EQUATIONS

In the incoherent case the mechanical equilibrium does not hold around dislocation cores when dislocations are created and when they are moving¹⁰. We thus need to set up the dynamic equation for the elastic displacement \mathbf{u} . In this paper the lattice velocity $\mathbf{v} = \partial \mathbf{u} / \partial t$ obeys the momentum equation⁹,

$$\rho \frac{\partial \mathbf{v}}{\partial t} = \eta_0 \nabla^2 \mathbf{v} + \nabla \cdot \vec{\sigma}. \quad (3.1)$$

The mass density ρ and the shear viscosity η_0 are constants. We neglect the bulk viscosity term ($\propto \nabla \cdot \mathbf{v}$) for simplicity¹⁰. In our model the sound waves relax owing to this viscous damping and the mechanical equilibrium $\nabla \cdot \vec{\sigma} = \mathbf{0}$ is rapidly attained unless η_0 is very small.

The composition obeys the diffusive equation,

$$\frac{\partial \psi}{\partial t} = \nabla \cdot \lambda(\psi) \nabla \frac{\delta F}{\delta \psi} \quad (3.2)$$

The kinetic coefficient depends on ψ as^{23,24}

$$\lambda(\psi) = \lambda_0(1 - \psi^2) = 4\lambda_0 c_A c_B, \quad (3.3)$$

where λ_0 is a constant. Here \mathbf{u} is fixed in the chemical potential difference $\delta F / \delta \psi$, so

$$\begin{aligned} \frac{\delta F}{\delta \psi} &= \frac{k_B}{v_0} \left[\frac{T}{2} \ln \left(\frac{1 + \psi}{1 - \psi} \right) - T_0 \psi \right] - C \nabla^2 \psi + \alpha e_1 \\ &+ \frac{\mu_{21}}{4\pi^2} [1 - \cos(2\pi e_2)] + \frac{\mu_{31}}{4\pi^2} [1 - \cos(2\pi e_3)] \end{aligned} \quad (3.4)$$

The last two terms arise from the elastic inhomogeneity. If $\lambda(\psi)$ is of the form of (3.3), the diffusion equation $\partial c_A / \partial t = D_0 \nabla^2 c_A$ ($\partial c_B / \partial t = D_0 \nabla^2 c_B$) follows in the dilute limit $c_A \rightarrow 0$ ($c_B \rightarrow 0$) with

$$D_0 = \lambda_0 k_B T v_0^{-1}, \quad (3.5)$$

where the coupling to the elastic field becomes negligible. In usual solid mixtures the diffusion is very slow and vacancies are in many cases crucial for a microscopic description of diffusion²⁴. Effects of such point defects are not treated in the present theory.

The total free energy $F_{\text{tot}} = F + \int d\mathbf{r} \rho \mathbf{v}^2 / 2$ including the kinetic energy then changes in time as

$$\frac{d}{dt} F_{\text{tot}} = - \int d\mathbf{r} \left[\sum_{ij} \eta_0 (\nabla_i v_j)^2 + \lambda(\psi) \left| \nabla \frac{\delta F}{\delta \psi} \right|^2 \right]. \quad (3.6)$$

Here the surface integrals have been omitted, which vanish if the boundaries are fixed and there is no flux of the atoms from outside (and also if the periodic boundary condition is imposed in simulations). The above time-derivative is non-positive-definite. As a result, the equilibrium is attained when $\mathbf{v} = \nabla \cdot \vec{\sigma} = \mathbf{0}$ and $\delta F / \delta \psi = \text{const}$.

Note that the dynamic equations (3.2) and (3.3) may be treated as Langevin equations with addition of the random noise terms related to the kinetic coefficients $\lambda(\psi)$ and η_0 via the fluctuation-dissipation relations⁴. However, we neglect the random noise in this paper, because we treat the effects insensitive to the thermal fluctuations.

IV. NUMERICAL RESULTS

A. Method

We integrated (3.1) and (3.2) in two dimensions on a 256×256 square lattice. The mesh size Δx was set equal to the lattice constant a in the reference state with $\mathbf{u} = \mathbf{0}$. This is needed to realize well-defined microscopic slips in our numerical scheme¹⁰. The system length is $L_0 = 256a$. The periodic boundary condition was imposed except the simulation of applying uniaxial deformation (Figs.13 and 14). Because the time scale of \mathbf{u} is shorter than that of ψ , we integrated (3.1) using an implicit Crank-Nicolson method. Space and time will be measured in units of a and

$$\tau_0 = (\rho / \mu_{20})^{1/2} a, \quad (4.1)$$

respectively, where μ_{20} is defined by (2.10) and $(\mu_{20}/\rho)^{1/2}$ is the transverse sound velocity propagating in the [11] direction. The free energies and the free energy densities are measured in units of $\mu_{20} a^2$ and μ_{20} , respectively. For simplicity, the scaled time $\tau_0^{-1} t$, position vector $a^{-1} \mathbf{r}$, and displacement vector $a^{-1} \mathbf{u}$ will be written as t , \mathbf{r} , and \mathbf{u} , respectively, in the same notation.

The dimensionless kinetic coefficients are given by

$$\lambda_0^* = \lambda_0 \tau_0 \mu_{20} a^{-2}, \quad \eta_0^* = \eta_0 / \tau_0 \mu_{20}. \quad (4.2)$$

In this paper we set $\lambda_0^* = 0.001$, $\eta_0^* = 0.1$, $K / \mu_{20} = 4.5$, $\alpha / \mu_{20} = 0.6$, and $k_B T_0 / v_0 \mu_{20} = 0.05$, where T_0 is the mean-field critical temperature in (2.4). Then $\lambda_0^* / \mu_0^* = D_0 \rho / \eta_0 \sim 10^{-2}$ and the diffusion time-scale of ψ becomes longer than the relaxation time-scale of the elastic field by two orders of magnitude. However, in real solid alloys, the time scale of the composition is much more

slower than that of the elastic field. Furthermore, we assume weak cubic anisotropy with $\mu_{30}/\mu_{20} = 1.1$ and weak elastic inhomogeneity with $\mu_{21} = \mu_{31} = 0.6\mu_{20}$.

In homogeneous one-phase states we have $e_2 = e_3 = 0$ and $e_1 = -\alpha\psi/K$. The well-known parameter $\eta = |\partial a/\partial\psi|/a$ defined by Cahn⁵ becomes $\eta = \alpha/2K = 0.067$, which represents the composition-dependence of the lattice constant a . The spinodal temperature T_s in (2.16) becomes 2.31.

B. Slips and composition changes

Edge dislocations appear in the form of slips or dipole pairs¹⁰, because a single isolated dislocation requires a very large elastic energy. Slips are thus fundamental units of plastic deformations. In Fig.2 we show the displacement and the composition around typical slips in a one-phase steady state with length $10\sqrt{2}a$ in the upper plate and $10a$ in the lower plate. Here we initially prepared a slip given by the linear elasticity theory¹⁰ at the critical composition ($\langle\psi\rangle = 0$) and let \mathbf{u} and ψ relax until the steady state was achieved. The temperature was kept at $T/T_0 = 2.5$ and no phase separation occurred. As in the previous simulations^{15,16}, we can see Cottrell atmospheres around the dislocation cores. The maximum and minimum of ψ at the lattice points close to the dislocation cores are of order ± 0.6 . Cottrell's result is obtained as follows: Let T be much higher than T_0 and α^2/L_0 and the gradient term be neglected (see (4.3)); then, the condition $\delta F/\delta\psi = \text{const.}$ yields $c_A/(1 - c_A) = \text{const.}$ $\exp(-U/k_B T)$, where $U = v_0\alpha e_1$ ²⁵. In our case the maximum of $|U|/k_B T$ at the lattice points is of order 1.

As a next step, starting with the configuration in Fig.2, we lowered the temperature to $T/T_0 = 2$ to induce spinodal decomposition. Subsequently the Cottrell atmospheres grew into domains and the dislocation cores stayed at the interface regions. The domain size attained finally was of order $50a$. Fig.3 illustrates the displacement and the composition in the final steady state, where the maximum and minimum of ψ are about ± 0.9 . Léonard and Desai¹⁴ obtained similar composition profiles in spinodal decomposition, where the elastic field of dislocations (given by the linear elasticity theory) was fixed in space and time.

Mathematically, slips in steady states satisfy $\delta F/\delta\mathbf{u} = \mathbf{0}$ and $\delta F/\delta\psi = \text{const.}$ Without externally applied strains, they are metastable owing to the Peierls potential energy arising from the discreteness of the lattice structure¹⁰. However, with increasing applied strain, they become unstable, leading to expansion or shrinkage of the slip length.

C. Dislocation formation around a hard domain

As in Fig.4, we created a single large hard (A-rich) domain at the center in the coherent condition at shallow

quenching $T/T_0 = 2$ after a long equilibration time. Here ψ is about 0.7 inside the domain and about -0.7 outside it. Its shape slightly deviates from sphericity owing to the weak cubic anisotropy assumed in this paper. We next performed a second deeper quenching to $T/T_0 = 1$. Subsequent diffusional adjustment of the composition proceeded very slowly, but a discontinuity of the order parameter $\Delta\psi$ about 1.8 was established relatively rapidly across the interface⁴. As a result, at a time about 1000 after the second quenching, the maximum of $|e_2|$ reached $1/4$, the value at stability limit, in the interface region (see the sentences below (2.7)). We then observed dislocation formation. The upper panel of Fig.5 shows the coherent elastic displacement \mathbf{u}_{coh} just before the dislocation formation, while the lower panel shows the subsequent additional incoherent change $\delta\mathbf{u} = \mathbf{u} - \mathbf{u}_{\text{coh}}$ after a time interval of 1000. In most cases, (i) two pairs of dislocation dipoles (four dislocations) appeared simultaneously in a narrow region, (ii) two of them glided preferentially into the softer region forming two slips perpendicular to each other, and (iii) slips collided in many cases and stopped far from the droplet, resulting in a nearly steady elastic deformation. Thus a half of the dislocation cores stay at the interface and the others are distributed around the domain. These three processes took only a short time of order 100.

After the above dislocation formation at a relatively early stage, the composition changed very slowly. We show three figures at $t = 23000$. Fig.6 displays the rotationally invariant strain,

$$e = (e_2^2 + e_3^2)^{1/2}, \quad (4.3)$$

The slips make an angle of $\pm\pi/4$ with respect to the x axis in the regions with large $|e_2|$ (in the uniaxially deformed regions), while they are parallel to the x or y axis in the corner regions with large $|e_3|$ ¹⁰. We also notice that the dislocation formation took place with the symmetry axis in the [11] direction for our special geometry. Fig.7 gives the free energy density f in (2.3), where the peaks represent the dislocation cores. In the interface region it exhibits a cliff arising from the gradient term and peaks arising from the dislocation cores. Fig.8 shows the order parameter ψ , where we can see Cottrell atmospheres around the dislocation cores surrounding the domain. The system is still transient and there is still a small composition flux through the interface.

D. Dislocation formation in a soft network

Next we examine dislocation formation when hard rectangular domains are densely distributed and wrapped by a percolated soft network. As in Fig.9, we prepared such a steady domain structure at $T/T_0 = 2$ in the coherent condition. As in the previous simulations^{21,22}, the hard domains (in gray) are elastically isotropic, while the soft network (in white) is mostly uniaxially stretched. That is, in the soft stripes between the two adjacent hard

domains, we obtain $e_2 \sim 0.2$ in the horizontal stripes and $e_2 \sim -0.2$ in the vertical stripes. We then quenched T to $T/T_0 = 1$ to induce the composition readjustment. Fig.10 displays the resultant time evolution of the total free energy $F = \int d\mathbf{r} f$ and the snapshots of e in (4.3) at the points A, \dots, E . It demonstrates that F mainly decreases due to the composition change but sometimes due to appearance and gliding of slips in the soft stripes. Note that the overall composition adjustment occurs slowly on the time scale of $R^2/D_0 = 10^5 - 10^6$ where R is the domain size. In Fig.11 we show the displacement \mathbf{u} within the square window in B, C and D, respectively, while in Fig.12 the bird views of the free energy density f are given at $t = 0$ and 4475 after the second quench. The peaks in Fig.12 represent the dislocation cores.

E. Work-hardening in two-phase states

Finally we apply a constant uniaxial deformation to initially coherent states with $\langle \psi \rangle = 0$ to induce plastic flow. That is, we set $u_x = u_y = 0$ at the bottom ($y = 0$) and $u_x = -u_y = \epsilon L_0/2$ at the top ($y = L_0$). The applied strain rate was fixed at $\dot{\epsilon} = 10^{-4}$, so $\epsilon = \dot{\epsilon}t$ with t being the time after application of the deformation. In Fig.13 we plot the average normal stress N_1 vs the applied strain ϵ for $T/T_0 = 3, 2.4$, and 2 (upper plate), where

$$N_1 = \langle \sigma_{xx} - \sigma_{yy} \rangle = \frac{1}{\pi} \langle \mu_2 \sin(2\pi e_2) \rangle. \quad (4.4)$$

The snapshots of e in (4.3) are also given at the points a, b, and c (lower plates). For $T/T_0 = 3$ the system is in a homogeneous one-phase state and random numbers with variance 0.01 were assigned to ψ at the lattice points at $t = 0$. In the initial state at $T/T_0 = 2.4$ the maximum and minimum of ψ and e_2 are ± 0.32 and ± 0.05 , respectively. At $T/T_0 = 2$ these numbers are magnified to ± 0.75 and ± 0.20 . All the initial states are coherent without dislocations. For $T/T_0 = 3$ the elastic instability occurs at $\epsilon = 1/4$ resulting in a fine mesh of slips as in the lower left plate. For $T/T_0 = 2.4$ the onset point of the slip formation is decreased to $\epsilon = 0.17$. For $T/T_0 = 3$ the onset is very early at 0.015, the stress-strain relation exhibits zig-zag behavior upon appearance of slips, and the stress continue to increase on the average (up to the upper bound of ϵ , 0.35, in the simulation). It is worth noting that this stress-strain curve resembles those of real two-phase alloys, where the monotonic increase of the stress without overshoot is characteristic of the work-hardening effect^{7,11,18}. Fig.14 consists of snapshots of e in (4.3) and the shear deformation energy density Φ in (2.7) in units of μ_{20} . We can see quadratic appearance of dislocations at the center of the uniaxially stretched stripes (top plate), gliding of the dislocations and pinning at the interfaces (top and middle plates), and thickening of the slips into *shear bands* (bottom plate)¹⁰.

V. SUMMARY AND CONCLUDING REMARKS

In summary, we have presented a coarse-grained phase field model of plastic deformations in two-phase alloys. The composition has been taken as a single order parameter. Extension of our theory is needed to more general phase separation processes involving an order-disorder phase transition^{2,4,14} and to diffusionless (Martensitic) structural phase transitions^{2,4}. Though our simulations have been performed in two dimensions, a number of insights into the very complex processes of plasticity have been gained. We mention them and give some remarks.

- (i) We have numerically examined dislocation formation around the interface regions, which occur spontaneously in deeply quenched phase separation.
- (ii) We have found that dislocations glide preferentially in the softer regions with smaller shear moduli and tend to be trapped in the interface regions.
- (iii) We have applied uniaxial strain to create multiple slips in two-phase alloys which were initially in the coherent condition. The dislocation formation starts in the mostly stretched middle points of the soft stripes. A stress-strain curve in Fig.13 at deep quenching is very different from the curves in one-phase states and exhibits the characteristics of work-hardened two-phase alloys^{7,11,18}.
- (iv) In our simulations without thermal random noise in the dynamics, the dislocation formation has taken place mostly at the mechanical instability condition $e \sim 1/4$. In real alloys, however, we should not neglect dislocations and point defects preexisting before quenching, around which the dislocation formation and extension by gliding can easily be triggered.
- (v) Dislocations move under applied strain. The dynamics is particularly complicated when they are coupled with an order parameter near its phase transition²⁶. Such problems could also be studied in our scheme.

Acknowledgments

We would like to thank Toshiyuki Koyama for valuable discussions on the incoherency effects in metallic alloys. This work is supported by Grants in Aid for Scientific Research from the Ministry of Education, Science, Sports and Culture of Japan.

Appendix

Here we assume weak elastic anisotropy and weak elastic inhomogeneity in the coherent condition in two dimensions, supposing shallow quenching. Then we may eliminate the elastic field in terms of ψ using the mechanical equilibrium condition $\nabla \cdot \vec{\sigma} = \mathbf{0}$ in the linear elasticity. We consider the space integral of the last two terms in the free energy density in (2.3): $\Delta F = \int d\mathbf{r} [\alpha e_1 \psi + f_{\text{el}}]$. We assume that $|\mu_{21}|$ and $|\mu_{31}|$ are much smaller than L_0 and that $\xi_a = 2(\mu_{20}/\mu_{30} - 1)$ is small, where $L_0 = K + \mu_{20}$.

Then ΔF may be rewritten as^{4,21,22}

$$\begin{aligned}\Delta F = & \int d\mathbf{r} \left[-\frac{\alpha^2}{2L_0} \psi^2 + \frac{1}{2} \tau_{\text{cub}} |\nabla_x \nabla_y w|^2 \right] \\ & + \int d\mathbf{r} \left[g_2 \psi (\nabla_x^2 - \nabla_y^2) w|^2 + g_3 \psi |\nabla_x \nabla_y w|^2 \right] \quad (\text{A.1})\end{aligned}$$

where w is obtained from the Laplace equation,

$$\nabla^2 w = \psi - \langle \psi \rangle, \quad (\text{A.2})$$

with $\langle \psi \rangle$ being the average order parameter. In the first line of (A.1) the bilinear terms are written with

$$\tau_{\text{cub}} = -(2\alpha^2/L_0^2)\mu_{20}\xi_a. \quad (\text{A.3})$$

The term proportional to τ_{cub} gives rise to anisotropic domains²⁰. The second line consists of the third-order terms with

$$g_2 = \mu_{21}\alpha^2/2L_0^2, \quad g_3 = 2\mu_{31}\alpha^2/L_0^2. \quad (\text{A.4})$$

The third-order terms are known to give rise to pinning of domain growth (and some frustration effects when g_2 and g_3 have different signs)^{21,22}.

In our simulations we set $\xi_a = 2(1/1.1 - 1) \cong -0.18$ and $\tau_{\text{cub}} \cong 0.0043\mu_{20}$, so the domains tend to become square or rectangular with interfaces parallel to the x or y axis. Furthermore, we set $g_2 = g_3/4 \cong 0.0035\mu_{20}$. For $\mu_{21} \sim \mu_{31}$ the typical domains in pinned two-phase states R_E is given by²¹

$$R_E \sim \gamma/[\mu_{21}(\Delta c)^3], \quad (\text{A.5})$$

where γ is the surface tension and Δc is the composition difference between the two phases. Thus R_E decreases as the quenching becomes deeper.

¹ J.W. Cahn, in *Critical Phenomena in Alloys, Magnets, and Superconductors*, edited by R.I. Jafee *et al.* (McGraw-Hill, New York, 1971), p.41.

² A.G. Khachaturyan, *Theory of Structural Transformations in Solids* (John Wiley & Sons, New York, 1983).

³ P. Fratzl, O. Penrose, and J.L. Lebowitz, *J. Stat. Phys.* **95**, 1429 (1999).

⁴ A. Onuki, *Phase Transition Dynamics* (Cambridge University Press, Cambridge, 2002).

⁵ J.W. Cahn, *Acta Metall.* **9**, 795 (1961).

⁶ J.W. Cahn, *Acta Metall.* **11**, 1275 (1963).

⁷ J.L. Strudel, in *Physical Metallurgy*, edited by R.W. Cahn and P. Haasen (North-Holland, Amsterdam, 1996), p.2106.

⁸ E. Nembach, *Particle Strengthening of Metals and Alloys* (Wiley, New York, 1997).

⁹ L.D. Landau and E.M. Lifshitz, *Theory of Elasticity* (Pergamon, New York, 1973).

¹⁰ A. Onuki, *Phys. Rev. E* **68**, 061502 (2003); *J. Phys. Condens. Matter* **15**, S891 (2003). In these papers a triangular lattice is assumed in two dimensions.

¹¹ A.H. Cottrell, *Dislocations and Plastic Flow in Crystals* (Clarendon Press, Oxford, 1953) ; A.H. Cottrell and M.A. Jaswon. *Proc. R. Soc. A* **199**, 104 (1949).

¹² J.W. Cahn, *Acta Metall.* **5**, 160 (1957).

¹³ A. A. Boulbitch and P. Tolédano, *Phys. Rev. Lett.* **81**, 838 (1998).

¹⁴ F. Léonard and R. Desai, *Phys. Rev. B*, **58**, 8277 (1988).

¹⁵ S.Y. Hu and L.Q. Chen, *Acta Mater.* **49**, 463 (2001); *Comput. Mater. Sci.* **23**, 270 (2002).

¹⁶ Y. Wang, D. J. Srolovitz, J. M. Rickman and R. LeSar, *Acta Mater.*, **48**, 2163 (2000).

¹⁷ S.Y. Hu, S. Schmauder, and L.Q. Chen, *Phys. Status Solidi. B* **220**, 845 (2000).

¹⁸ A.S. Argon, in *Physical Metallurgy*, edited by R.W. Cahn and P. Haasen (North-Holland, Amsterdam, 1996), p.1878, 1958; P. Haasen, *ibid.* p.2010.

¹⁹ C. Saguí, A. M. Somoza and R.C. Desai, *Phys. Rev. E* **50**, 4865 (1994).

²⁰ H. Nishimori and A. Onuki, *Phys. Rev. B* **42**, 980 (1990).

²¹ A. Onuki and H. Nishimori, *Phys. Rev. B* **43**, 13649 (1991); A. Onuki and A. Furukawa, *Phys. Rev. Lett.* **86**, 452 (2001).

²² D. Orlikowski, C. Saguí, A. M. Somoza and C. Roland, *Phys. Rev. B* **59**, 8646 (1999); *ibid.* **62**, 3160 (2000).

²³ K. Kitahara and M. Imada, *Prog. Theor. Phys. Suppl.* **64**, 65 (1978).

²⁴ K. Binder, in *Material Sciences and Technology* ed. R. W. Cohen, P. Haasen and E.J. Kramer (VCH, Weinheim, 1991), Vol. 5.

²⁵ The linear elasticity theory⁹ yields $e_1 = \text{const.}y/(x^2 + y^2)$ for a single edge dislocation at the origin. The expression for a slip is obtained in the presence of two dislocations with opposite Burgers vectors. See Ref.[10].

²⁶ A. L. Korzhenevskii, R. Bausch, and R. Schmitz, *Phys. Rev. Lett.* **91**, 236101 (2003).

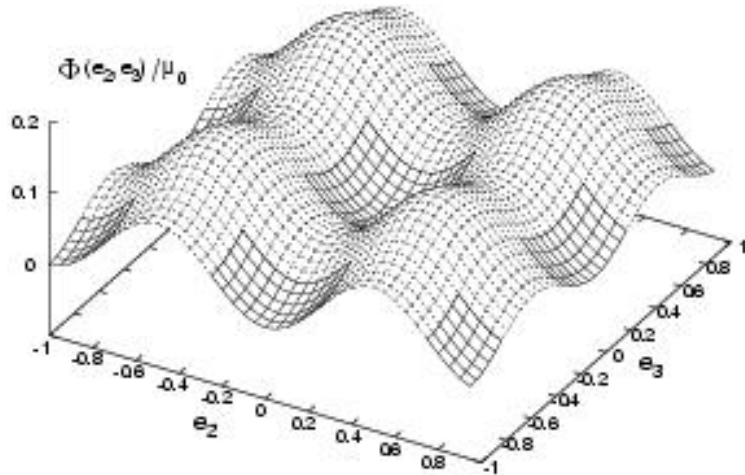


FIG. 1: Normalized shear deformation energy $\Phi(e_2, e_3)/\mu_0$ for the case $\mu_2 = \mu_3 = \mu_0$. The elastically stable regions are meshed with solid lines on the surface.

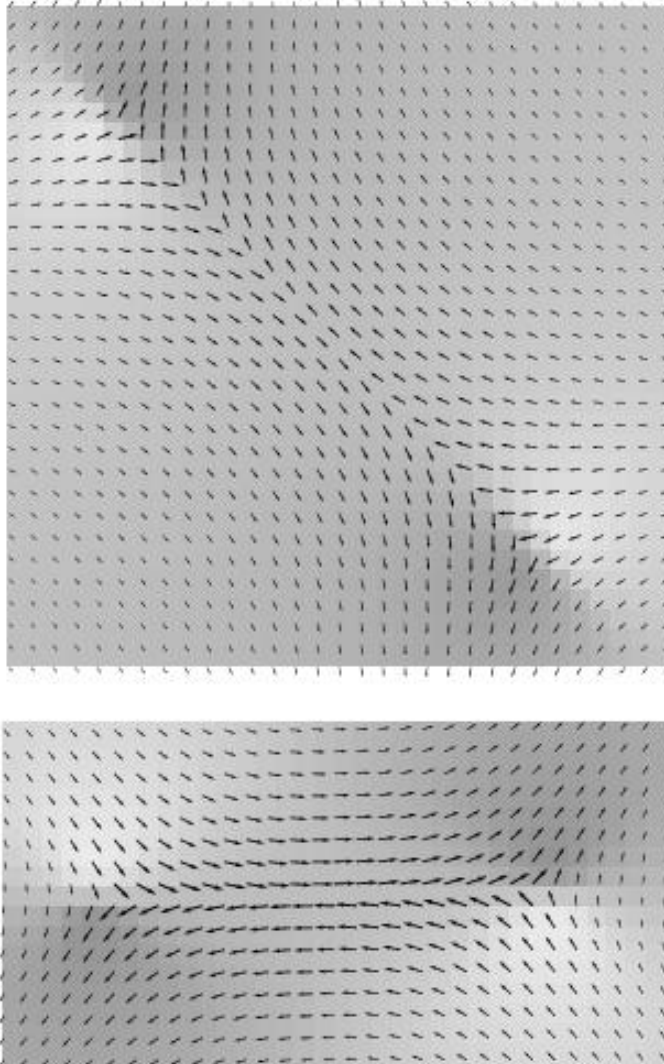


FIG. 2: Displacement vector for a slip (dislocation pair) making an angle of $3\pi/4$ (upper plate) and 0 (lower plate) with respect to the x (horizontal) axis in a one-phase steady state at $T/T_0 = 2.5$. The degree of darkness represents the composition.

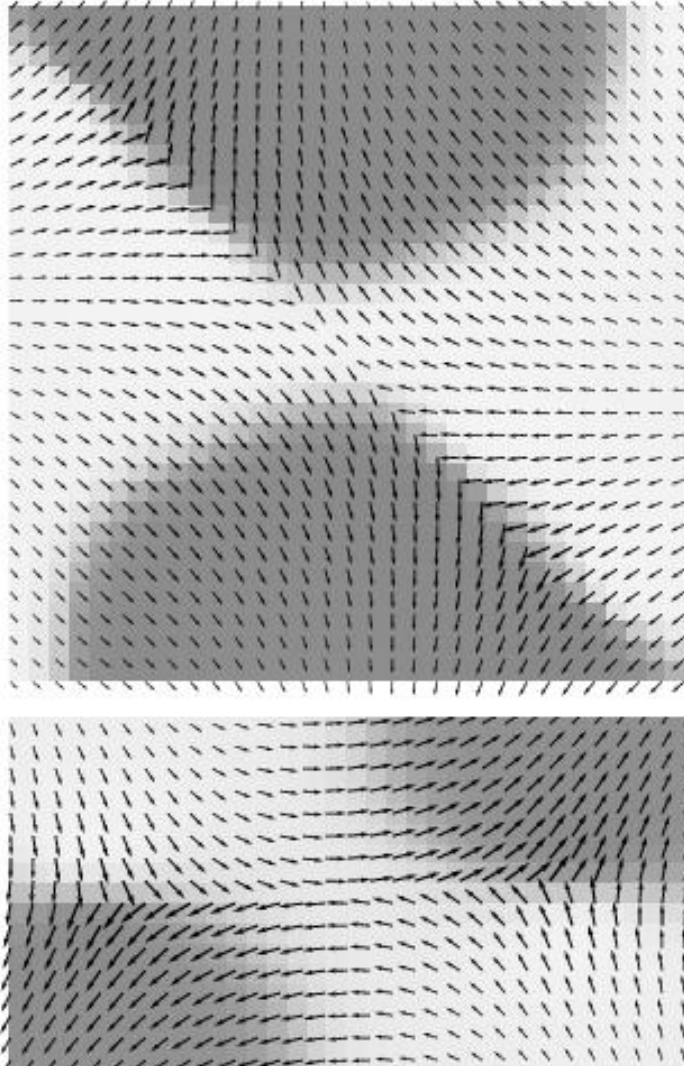


FIG. 3: Displacement vector for a slip (dislocation pair) in a two-phase steady state at $T/T_0 = 1.7$ obtained from the configuration in Fig.2 after quenching. The dislocation cores are trapped at the interface regions.

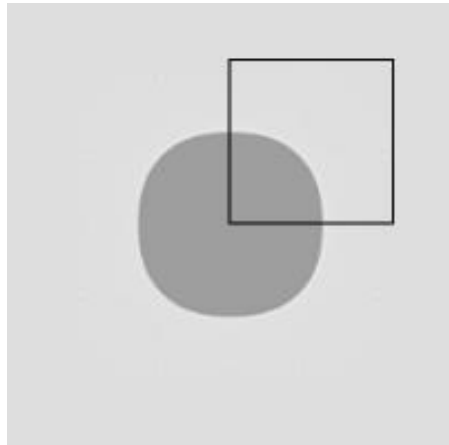
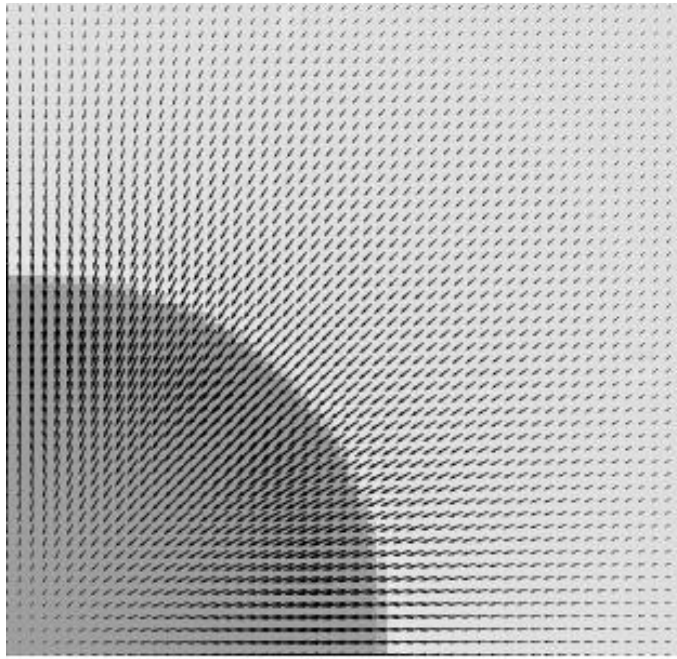
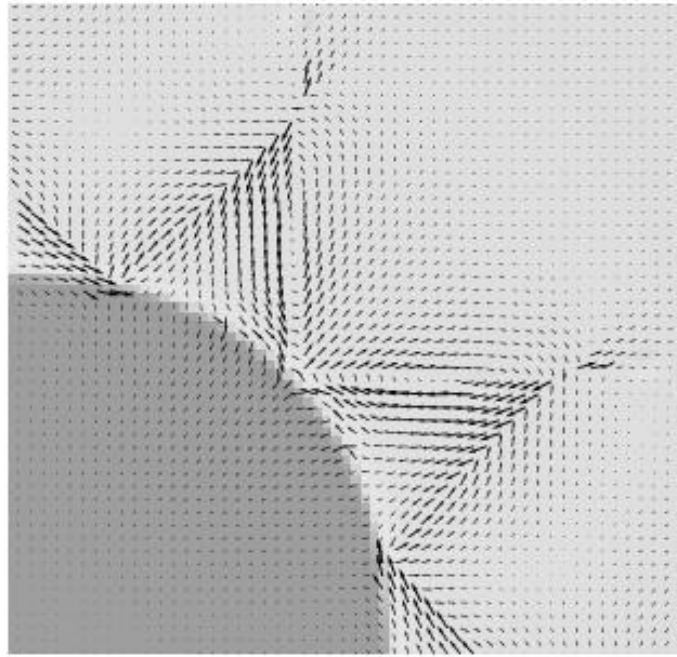


FIG. 4: Hard domain in a steady state at $T/T_0 = 2$. The displacement in the square region will be displayed in Fig.5.



\mathbf{u}_{coh}



$\mathbf{u} - \mathbf{u}_{coh}$

FIG. 5: Upper plate: Coherent elastic displacement \mathbf{u}_{coh} just before birth of dislocations at deep quenching at $T/T_0 = 1$. Right: Incoherent elastic displacement after appearance of dislocations.

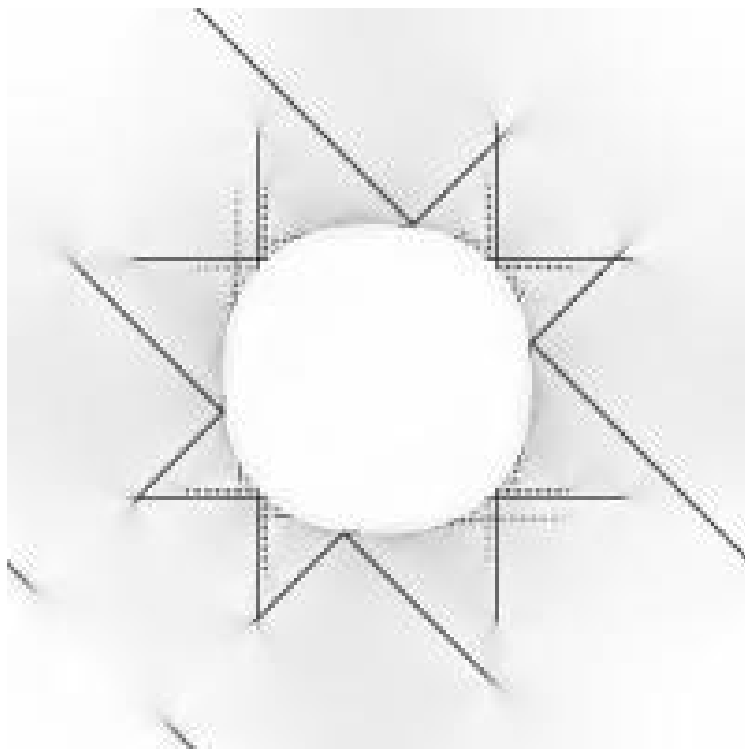


FIG. 6: Snapshot of e in (4.3) after dislocation formation, which is zero within the hard domain and nonvanishing outside. The slip lines end at dislocations.

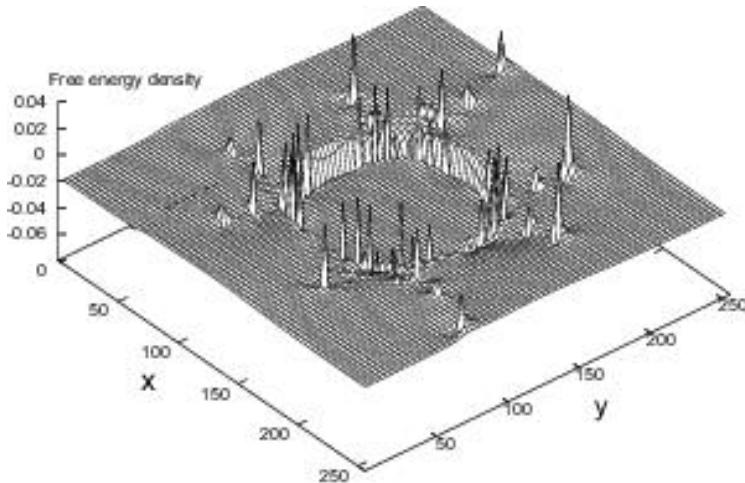


FIG. 7: Snapshot of the free energy density f in (2.3). The peaks are located near the dislocation cores and the cliff represents the interface free energy density.

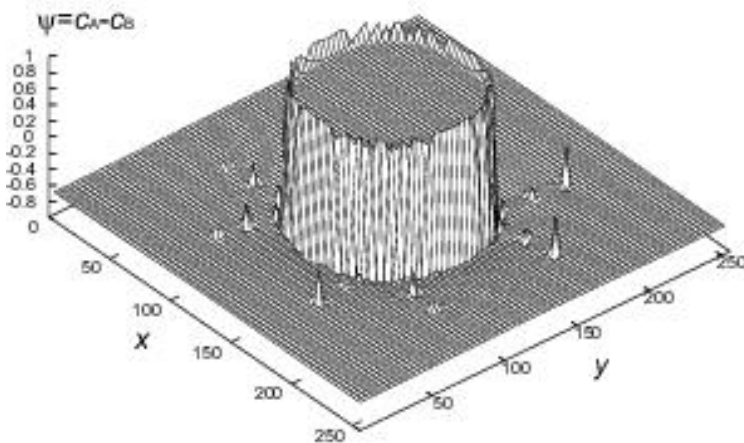


FIG. 8: Snapshot of the order parameter around the hard domain in the incoherent case obtained by a two-step quench. The small cliff at the interface arises because the system is still in a transient state. The peaks around the dislocation cores in the outer soft region represent Cottrell atmospheres.

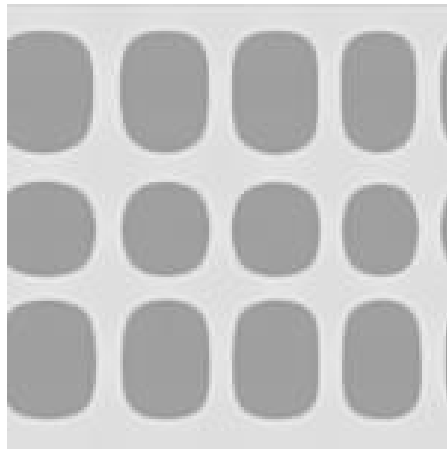


FIG. 9: Domain structure obtained at shall quench $T/T_0 = 2$ in the coherent condition.

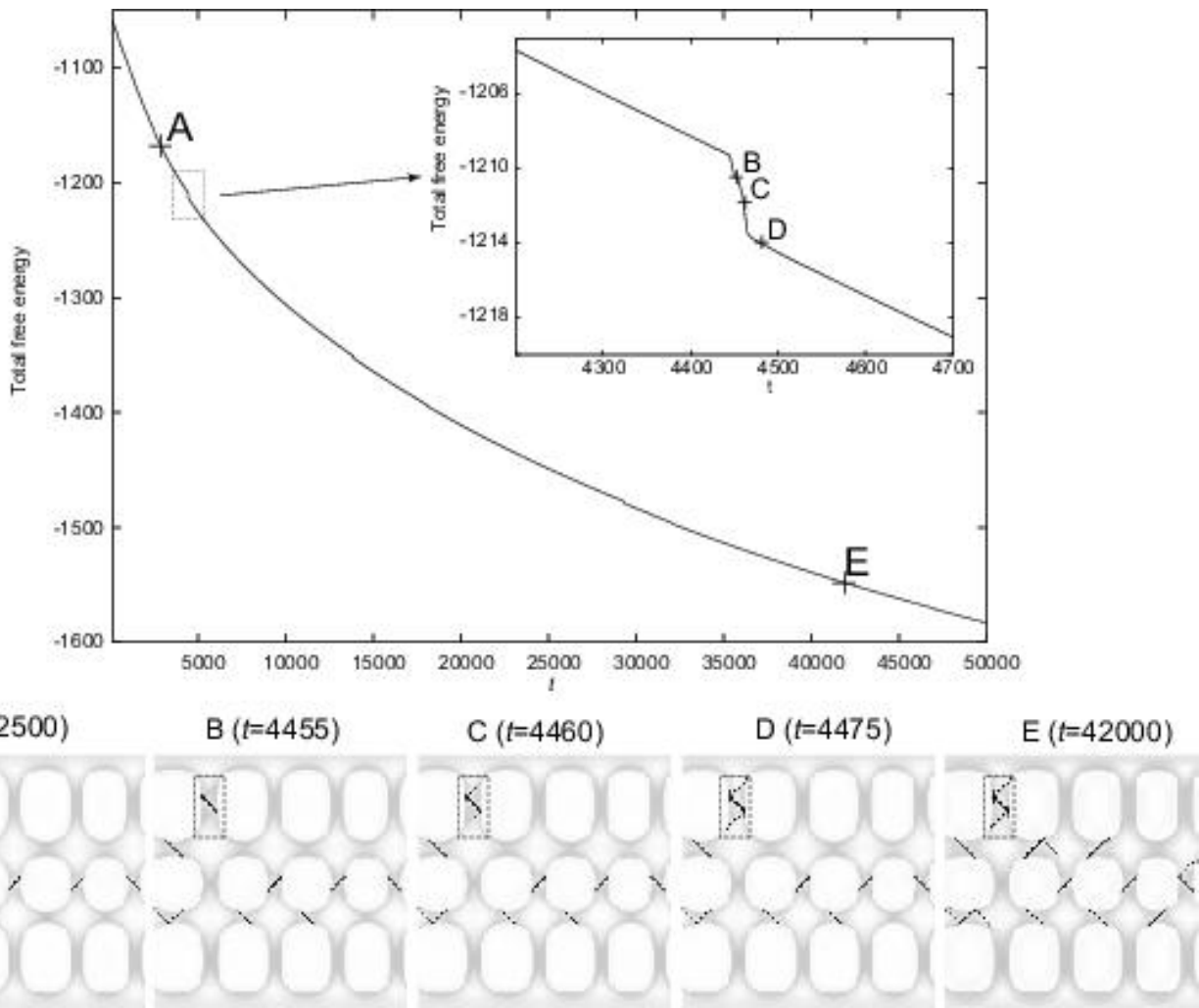


FIG. 10: Relaxation of the total free energy F after a two-step quench from $T/T_0 = 2$ to 1 with the initial configuration in Fig.9. It mostly relaxes due to the composition adjustment, but it sometimes relaxed due to dislocation formation as enlarged in the inset. Snapshots of e of the points A \sim E are given below.

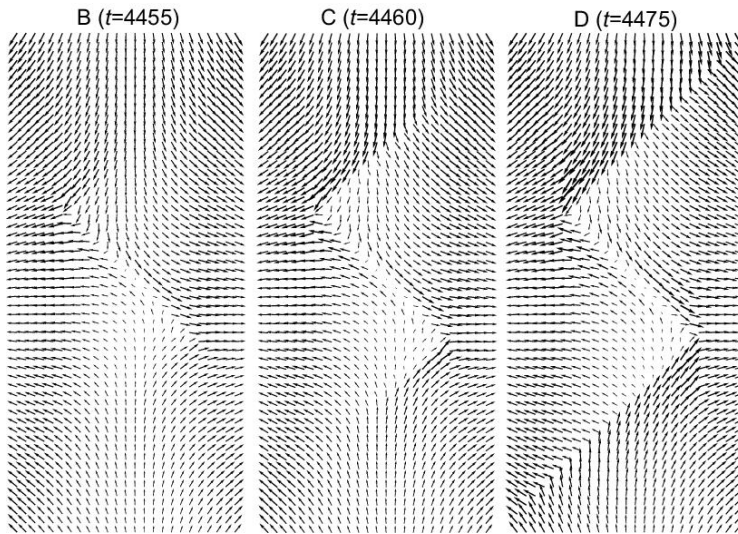


FIG. 11: Elastic displacement u in the marked regions B,C, and D.

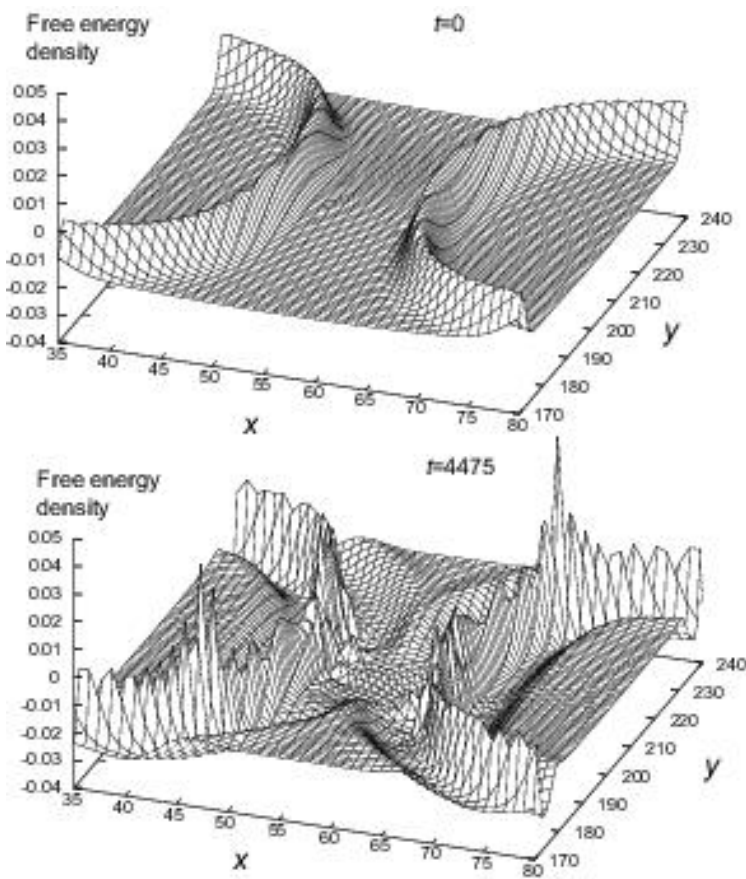


FIG. 12: Bird views of the free energy density f at $t = 0$ and 4475 after the two-step quench.

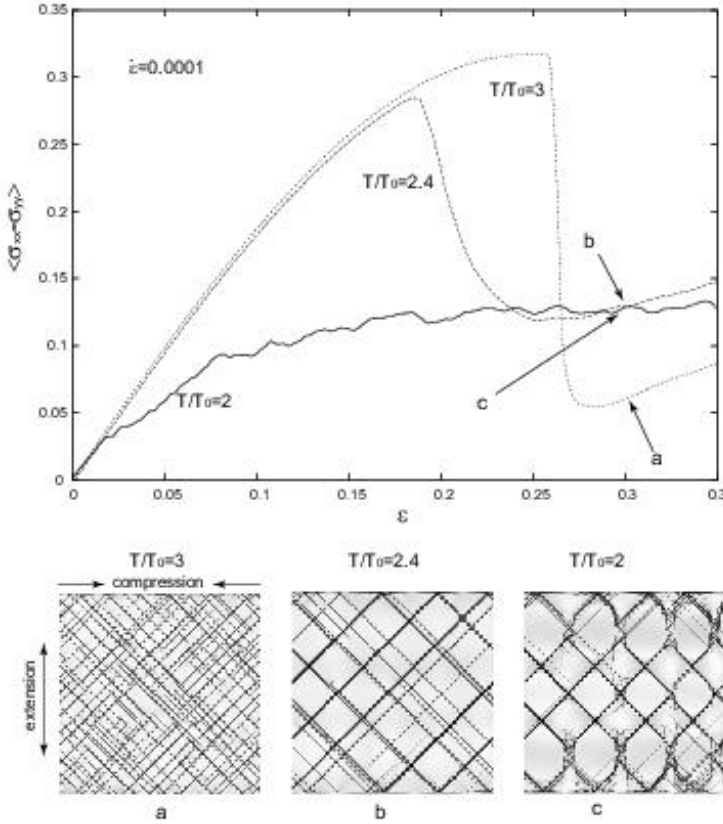


FIG. 13: Stress-strain curves after application of uniaxial stretching at $\dot{\epsilon} = 10^{-4}$ for $T/T_0 = 3, 2.4$, and 2 . Snapshots of e in (4.3) at points a,b, and c are given below, which represent slip patterns in plastic flow.

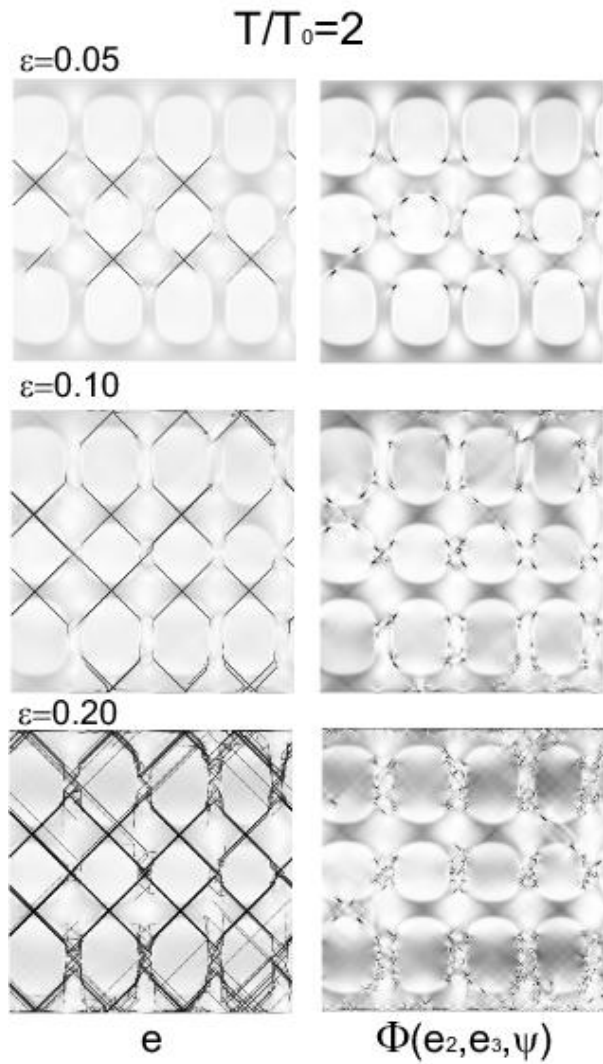


FIG. 14: Snapshots of e in (4.3) and the shear deformation energy density Φ in (2.7) at $T/T_0 = 2$ for $\epsilon = 0.05, 0.1$, and 0.2 .